Radiation damage and evolution of radiation-induced defects in Er_2O_3 bixbyite

2009 J. Phys.: Condens. Matter 21 115403

(http://iopscience.iop.org/0953-8984/21/11/115403)

J. Phys.: Condens. Matter **21** (2009) 115403 (11pp) doi:10.1088/0953-8984/21/11/115403

Radiation damage and evolution of radiation-induced defects in Er_2O_3 bixbyite

L Kittiratanawasin[1], Roger Smith[1], B P Uberuaga[2] and K E Sickafus[2]

[1] Department of Mathematical Sciences, Loughborough University, Loughborough, Leicestershire LE11 3TU, UK
[2] Los Alamos National Laboratory, Los Alamos, NM 87545, USA

Received 19 December 2008, in final form 19 January 2009
Published 19 February 2009
Online at stacks.iop.org/JPhysCM/21/115403

Abstract

Collision cascade simulations were performed in the Er_2O_3 sesquioxide. The resulting point defects observed at the end of the ballistic phase of the collision cascade were analysed and their evaluation over longer time examined using temperature accelerated dynamics and the kinetic Monte Carlo method. The result shows that the large mass difference between the Er and O atoms results in cascades with different structures where an initially energetic O atom can channel over long distances, depositing energy in smaller sub-regions, whereas denser cascades with vacancy-rich cores develop from Er primary knock-on atoms. The most mobile defect that can form is the isolated O vacancy but when this occurs as part of a larger defect cluster it becomes trapped. The energy barriers for all other defects to move are very high.

(Some figures in this article are in colour only in the electronic version)

1. Introduction

The search for radiation-tolerant materials is a topic that is of increasing importance as these materials have the potential to be used as containment matrices for radioactive waste and could be candidate materials for the inert matrix used for actinide transmutation and plutonium burning [1]. Previous work by us has examined the radiation damage that can occur in MgO [2, 3] and magnesium aluminate spinel, $MgAl_2O_4$ [4–7]. In the latter case the material was found to have the ability to incorporate large numbers of cation antisite defects which is one of the reasons for its relative tolerance to radiation. In the former case the vacancies were found to be relatively immobile at room temperature but the isolated interstitial and di-interstitial defects could diffuse at room temperature and even some larger interstitial clusters were relatively mobile. The so-called 'rare earth oxides' are another class of oxide materials that could be radiation-tolerant. They differ from the previously studied materials not just in their basic crystal structure but also because of the large mass difference between the two atomic species.

The purpose of this investigation is to determine the mechanisms of radiation damage in the rare earth sesquioxide, Er_2O_3, which has the bixbyite structure, by means of molecular dynamics computer simulation with a view to explaining the experimental observations of radiation damage response in bixbyite. The experimental investigation of heavy-ion-irradiated bixbyite shows that this crystal is relatively tolerant to radiation but that under high doses (≈5–25 dpa) of 300 keV heavy ions the structure can transform from a cubic (C phase) to a monoclinic (B phase) structure with a corresponding density increase of about 9% [8–11]. Moreover, an intermediate phase, a disordered fluorite structure, is found at low ion doses (≈2.5 dpa) before the transformation to the B phase at a higher irradiation dose [12, 13].

Some preliminary work on the simulation of radiation effects in Er_2O_3 [14] identified the main types of point defects that can arise and showed that there was a substantial difference between a radiation event that triggered an erbium primary knock-on atom (PKA) compared to an oxygen PKA. The large mass difference resulted in much more channelling and sub-cascades in the latter case, with damage occurring primarily on the O sub-lattice. In addition the energy barriers for isolated point defects to diffuse were much higher than in MgO and $MgAl_2O_4$. In these cases the interstitials were more mobile whereas, in the case of Er_2O_3, the O vacancy had the lowest

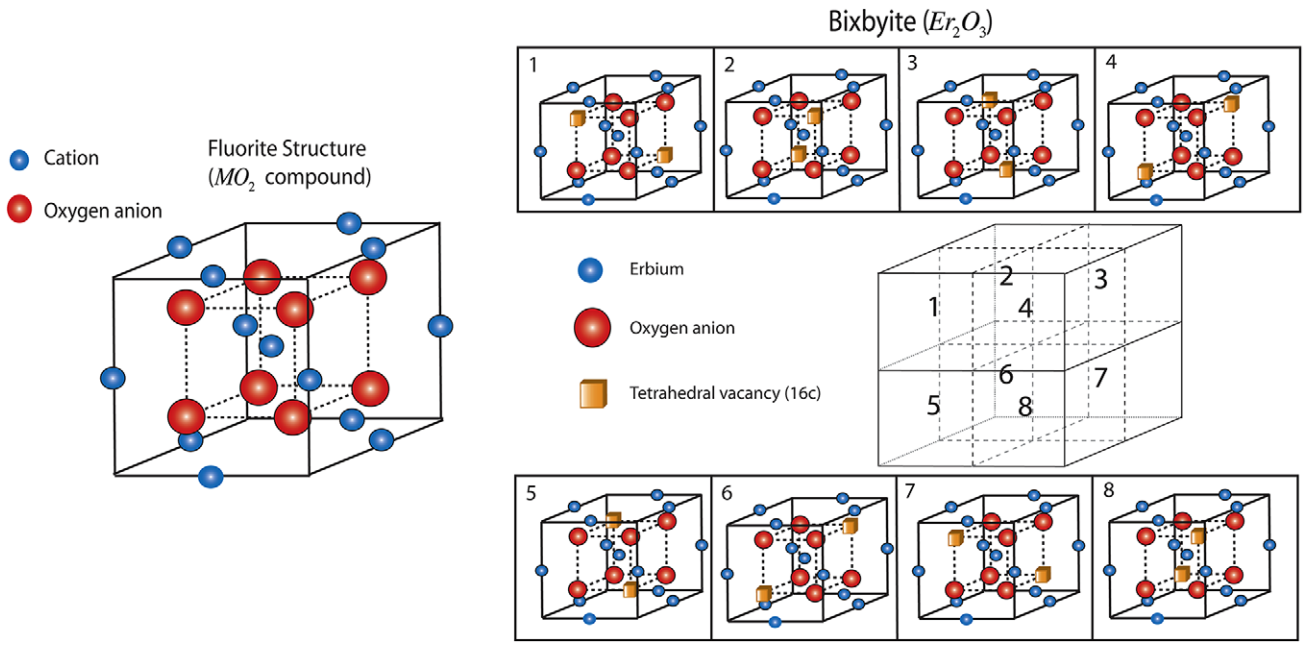

Figure 1. (Colour online) A comparison of the bixbyite and fluorite structures. The eight units with O atoms at the vertices will be referred to as oxygen sub-cubes. The similarity of the structures is best seen by comparing the larger sub-cubes with the cations on their edges to the fluorite structure.

barrier. Here we examine these effects in more detail with better statistics and use long timescale simulation techniques to investigate defect mobility and diffusion.

2. Methodology

2.1. Molecular dynamics simulations

At room temperature, the sesquioxide Er_2O_3 exhibits the cubic bixbyite (C phase, space group $Ia\bar{3}$) structure. The unit cell of Er_2O_3 is composed of 32 erbium (occupying the 8a and 24d equipoints) and 48 oxygen atoms (occupying the 48e equipoints) with a lattice constant of 1.055 nm. In this structure, the Er atoms approximately lie in a face centred cubic arrangement while the O atoms occupy three-quarters of all the tetrahedral interstices. The bixbyite structure is closely related to the fluorite structure. The difference is shown in figure 1. Apart from rotational symmetry, the bixbyite structure has two tetrahedral vacancies (16c) at the corners of the oxygen cube.

Molecular dynamics (MD) simulations are used to investigate radiation damage from collision cascades. The model for the interatomic potential is based on fixed charges with the pairwise-additive potential energy function, composed of a standard Buckingham potential and an electrostatic potential. The details of the potential parameters are given in [15]. These parameters give an equilibrium lattice constant of 1.052 nm, compared to the experimental value of 1.055 nm. The elastic properties of the potential were not tested. The simulation was carried out using fixed boundaries (i.e. the outer three layers of Er atoms and the outer two layers of O atoms) and the fast multipole method was used to calculate the Coulomb sums [16]. Periodic boundary conditions were not imposed but tests were carried out to check that energetic particles did not enter the fixed embedded region and that atoms outside this region were at their equilibrium lattice sites before the start of the simulation. This method is chosen for computational efficiency reasons. Radiation events were initiated by imparting kinetic energy in different directions to a PKA, somewhere near the centre of the cubic bixbyite structure at 0 K. We investigate PKAs with initial energies of 0.4, 2 and 10 keV. The system sizes for running the collision cascades varied between 10 300 atoms to 1112 832 atoms in a cubic box whose size was chosen so that the defects which formed were well separated from the boundaries. At 0.4 keV, 42 different trajectories were run; at 2 keV, 20 separate PKAs were considered but at 10 keV data were only analysed for the Er PKA from 10 separate cascades. This is because a lattice containing even 1112 832 atoms could not contain the 10 keV collision cascade from an O PKA, independent of the initial direction. No thermostat was used so the initial temperature of the lattice was 0 K but the overall system temperature could rise up to 40 K for the higher energy O and Er PKAs at the end of the simulation. For the 2 keV Er PKA where a smaller system was used the final temperature was 190 K and somewhat higher for the smaller 400 eV simulations due to the small lattice size. In order to analyse the radiation damage, vacancies and interstitials need to be defined. An interstitial is defined as an atom that resides at a site which is further than 0.86 Å (just over one-third of nearest-neighbour spacing in the ideal lattice) from any lattice site in the original system. Conversely, a vacancy is defined as a site in the original lattice which has no atom lying closer than 0.86 Å.

Table 1. The average number of defects left at the end of the ballistic part of the collision cascade, per cascade averaged over 21 individual cascades for the 400 eV simulations and 10 individual cascades for the others.

PKA energy	0.4 keV O	0.4 keV Er	2 keV O	2 keV Er	10 keV Er
Average number of Er vacancies per PKA	0	1.5	4	7	25
Average number of O vacancies per PKA	1.5	2.3	11	15	77

2.2. Temperature accelerated dynamics

MD simulations are limited by the timescale that can be simulated (≈1 ns for system sizes containing a few thousand atoms). In order to understand the longer time evolution of defects, we have performed temperature accelerated dynamics (TAD). TAD, introduced by Sørensen and Voter *et al* [17], is a method to reach longer timescales than possible with MD for systems characterized by rare events. The basic concept involves reducing the waiting time between events by raising the temperature to some temperature, T_{high}, higher than the temperature of interest T_{low}. However, doing this directly disrupts the relative probability of the system following one pathway versus another. Therefore, the times of events seen at T_{high} are extrapolated to T_{low}. This extrapolation requires the energy barrier for the event, found here using the nudged elastic band (NEB) method [18], and is exact if the system obeys harmonic transition state theory. The TAD algorithm consists of performing MD at T_{high}. The trajectory is monitored for escapes from the current state of the system, defined as an energy basin in the potential energy surface. Once an escape occurs, the time for that escape at T_{high}, t_{high}, and the barrier E_{ij} are determined and the system is placed back into the original energy basin. The time for that escape attempt is extrapolated to T_{low} via the equation

$$t_{\text{low}} = t_{\text{high}} \mathrm{e}^{E_{ij}\left(\frac{1}{k_{\text{B}}T_{\text{low}}} - \frac{1}{k_{\text{B}}T_{\text{high}}}\right)} \tag{1}$$

where k_{B} is the Boltzmann constant. This procedure is continued until a stopping criterion is met, defined by the time

$$t_{\text{high,stop}} = \frac{\ln(1/\delta)}{\nu_{\text{min}}} \left(\frac{\nu_{\text{min}} t_{\text{low,short}}}{\ln(1/\delta)} \right)^{T_{\text{low}}/T_{\text{high}}}. \tag{2}$$

Here, $t_{\text{low,short}}$ is the shortest extrapolated time for all events at T_{low}, ν_{min} is an assumed minimum prefactor in the system and δ is a user-supplied confidence or probability that, if the high temperature MD were continued, some other event could extrapolate to an even shorter time at T_{low}. Once $t_{\text{high,stop}}$ is reached at the high temperature, the event with the shortest time $t_{\text{low,short}}$ is accepted, the system moved in the corresponding state and the clock advanced by $t_{\text{low,short}}$. The procedure is then repeated for the new state. If harmonic transition state theory is valid for the system being studied, TAD will give exact state-to-state dynamics.

In this work T_{high} was set to 3000 K and T_{low} was varied between 300 and 2000 K depending on the rate of movement and the amount of computer time consumed in performing the calculation. ν_{min} and δ were chosen at 10^{12} and 0.05, respectively. Only isolated point defects typically observed in the collision cascade were analysed. As a result a much smaller lattice size could be used for the TAD simulations. The chosen lattice contained 640 atoms.

2.3. Kinetic Monte Carlo (KMC)

Having determined the energy barriers and prefactors (ν_0) for all possible transitions of a point defect in a perfect lattice, KMC can be used to track the motion of these defects and to determine the diffusion constants. If there are n possible transitions for a point defect to move from state i, the relative probability for a transition to state j is given by

$$\rho_{ij} = \frac{r_{ij}}{\sum_{j=1}^{n} r_{ij}} \tag{3}$$

where r_{ij} is the rate constant for moving from state i to state j. The system is moved to state j if $\sum_{k=1}^{j-1} \rho_{ik} < R_0 < \sum_{k=1}^{j} \rho_{ik}$, where $R_0 \in (0, 1)$ is a uniformly distributed random number. The KMC simulation time for that move can be obtained by generating another uniformly distributed random number $R \in (0, 1)$ and advancing the simulation time clock by a time Δt given by

$$\Delta t = -\frac{\ln R}{\sum_{j=1}^{n} r_{ij}}. \tag{4}$$

KMC is used here to calculate the diffusion constant D of a point defect with predetermined energy barriers calculated from TAD via

$$D = \frac{\langle |r|^2 \rangle}{6 t_{\text{sample}}} \tag{5}$$

where r is the displacement of the defect during the t_{sample} interval time. Typically millions of KMC steps are performed for a time $t_{\text{run}} = m t_{\text{sample}}$ and the values of t_{sample} are varied along with the value of the number of time intervals m until good convergence for the value of D is achieved.

3. Collision cascade simulations

The calculated number of defects left at the end of the ballistic phase of the cascades is given in table 1. At all energies the Er PKA produces more damage than the O PKA. At 400 eV the O PKA produces damage only on the O sub-lattice, mostly in the form of isolated O interstitials and vacancies, except in the case of a direct head-on collision with an Er ion. Snapshots of typical cascades from a 400 eV Er PKA and a 400 eV O PKA are shown in figure 2. This shows that the Er PKA produces a di-vacancy and a split Er interstitial next to an O interstitial, whereas the O PKA leaves two isolated O vacancies and interstitials.

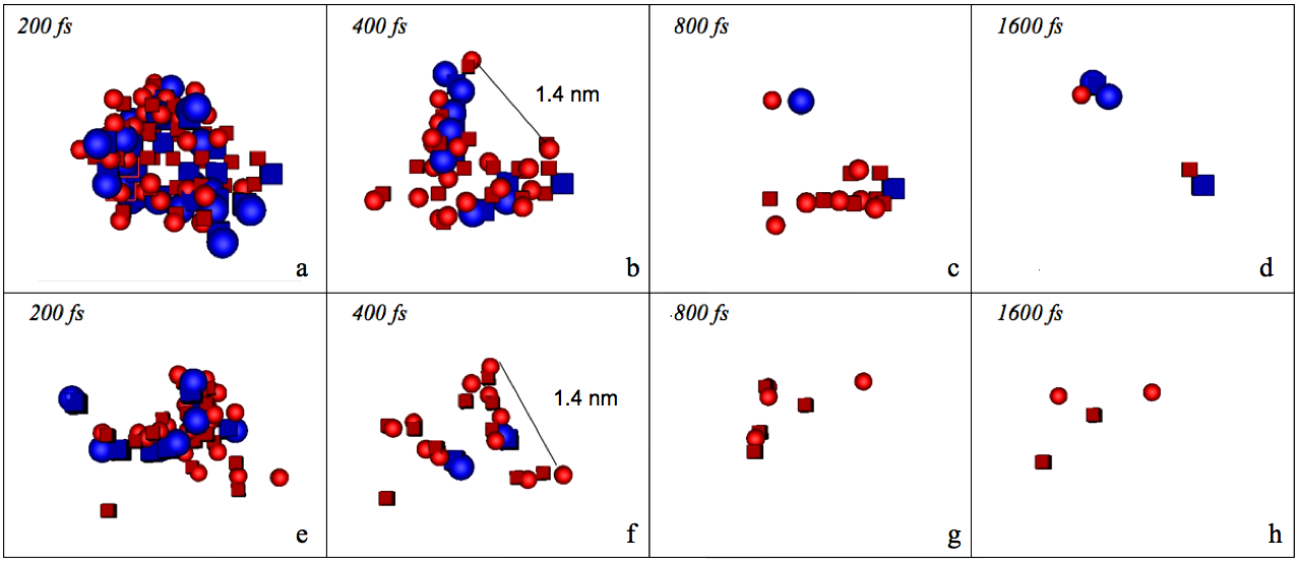

Figure 2. (Colour online) Snapshots from typical 400 eV collision cascades for an Er PKA ((a)–(d)) and an O PKA ((e)–(h)) at times of 200, 400, 800 and 1600 fs. The colour code and symbol key used in this figure also applies to all other figures. Small cubes represent O vacancies and large cubes refer to Er vacancies. The larger spheres represent Er interstitials and the small spheres are O interstitials.

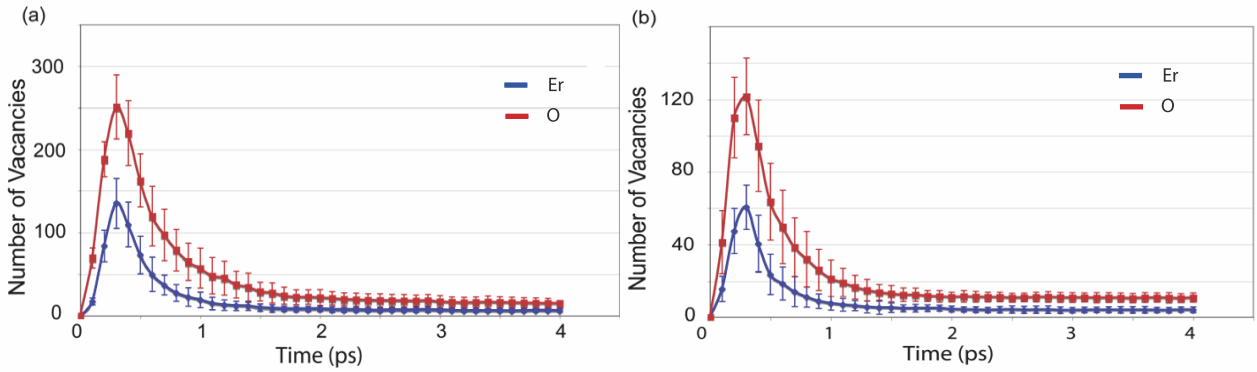

Figure 3. (Colour online) The evolution of defects as a function of time in 2 keV collision cascades for the (a) Er PKA and (b) O PKA, each averaged over 10 separate PKA directions.

At 2 keV the main differences observed between the Er and O PKA are in the number of retained defects and the distance over which the cascade spreads. Er PKAs cause more damage than O PKAs (see figure 3) and the spatial spread of the Er PKA collision cascades is less. For the Er PKA, there are Er vacancies along the initial PKA track, with the majority of Er interstitials around the edge of the damage zone. The O defects are, on average, distributed fairly evenly throughout the damage region. O PKA cascades result in sub-cascade branching and spatially separated damage over long distances as shown in figure 4.

This can be explained by the fact that the lighter O atoms are easily scattered by the heavier Er atoms, thus transferring less energy. This causes the O PKA to move a longer distance and to initiate small sub-cascades along its path.

Typical defects from the cascades were categorized and are described in figure 5. Most O interstitials are located at the tetrahedral 16c site but there were a few cases where the O interstitial positioned itself between two structural vacancies. The displaced Er atoms can form either as a split Er interstitial occupying the empty O vertices in the O sub-cube or as an isolated Er interstitial (0.18 eV higher in energy) occupying only one of the vertices. An Er interstitial can also occur with one or two O interstitials to form a di-or tri-interstitial cluster. Both the isolated Er vacancy and the Er–O di-vacancy have the missing Er atom in the 8a position. No isolated Er vacancies were found at the 24d lattice point. The O-square defect referred to in the caption of figure 5 is a defect where two O atoms swap with the two structural vacancies in one of the cubic sub-units shown in figure 1. These defects commonly occur and are discussed in more detail later.

The collision cascades formed by Er PKAs produce more damage than O PKAs since they can transfer kinetic energy more efficiently to surrounding atoms. For the 10 keV collision cascade, the simulations were performed only with Er PKAs. In this case the peak damage occurs between 0.5 and 0.6 ps after the start of the cascade, somewhat later than at 2 keV. Defects remaining after the ballistic phase of a typical 10 keV

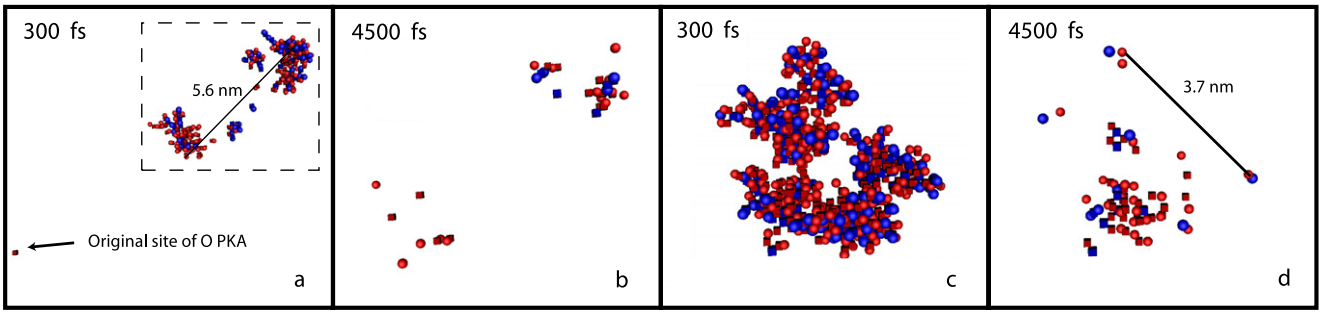

Figure 4. (Colour online) Snapshots of 2 keV collision cascades initiated by the O and Er PKA along ⟨123⟩ and ⟨253⟩ directions, respectively. (a) and (c) show the damage after 0.3 ps for the O and Er PKA, respectively. (b) and (d) show the damage for the O and Er PKAs after the ballistic phase of the cascade (4.5 ps). The dotted region outlined in (a) is shown in (b).

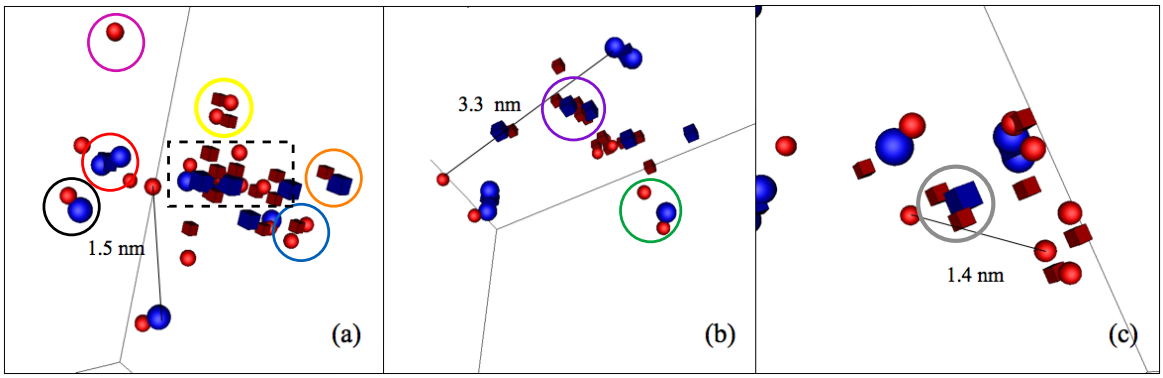

Figure 5. Typical defects from 2 keV collision cascades. (a) shows a di-interstitial (the leftmost circle), an isolated oxygen interstitial (top circle), a split Er interstitial (second circle from left), the O square defect (second circle from top), a split O interstitial (second circle from right) and a divacancy (rightmost circle). In the rectangle there is a disordered region which is difficult to categorise in terms of simple defects. (b) shows a tri-interstitial (bottom circle) and a five-vacancy cluster (top circle). A trivacancy is shown circled in (c).

collision cascade are shown in figure 6. The defects are located in a region of the crystal that roughly follows the initial path of the PKA. It can be seen that the Er defects tend to be more isolated than the O defects and that there is some disordering of the O sub-lattice along the paths of the most energetic recoils (figure 7). It is hard to identify these regions as disordered fluorite, as observed experimentally at low doses. The radiation damage in the bixbyite structure is different from that observed with our previous work in MgO and normal spinels where the damage consisted mostly of separated point defects. On the other hand, there is not the same extended amorphization of the damage region observed with cascades in zircon and the titanate pyrochlores [19, 20].

4. Kinetics of point defects

In order to have greater understanding of the longer time evolution of the radiation damage in Er_2O_3 we examine the point defects in more detail and investigate their movement using temperature accelerated dynamics (TAD). For this investigation a lattice size containing 640 atoms is used with T_{high} at 3000 K and T_{low} varying between 300 and 2000 K, depending on the type of defect and the magnitude of the energy barrier.

4.1. Oxygen vacancy

Of all the point defects investigated, the oxygen vacancy has the smallest energy barrier for diffusion. The minimum transition energy barrier is 0.81 eV and the pathway is shown in figure 8 along with the other pathways investigated. In order for the O vacancy to diffuse through the lattice a barrier greater than 0.81 eV needs to be overcome, since the lowest energy barrier has only one pathway in every position. Thus net diffusion occurs only as a result of overcoming the second-lowest energy barrier, not the lowest, i.e. the barrier for diffusion is 1.01 eV. Figures 8(a)–(c) show the pathways with barriers of 0.81, 1.01 and 1.37 eV. These transitions occur via a direct exchange of the oxygen vacancy with a neighbouring oxygen atom. The last three energy barriers are rarer events with higher energy barriers of 1.94, 1.97 and 2.31 eV (see figures 8(d)–(f)). Rather than a direct exchange mechanism, these movements use the lattice vacancy (16c) as an intermediate site to which the replacing oxygen first moves. These latter transitions are rare even at high temperatures. The energy barriers, together with the number of transition pathways, are given in table 2 for both the O vacancy and O interstitial. This is discussed below.

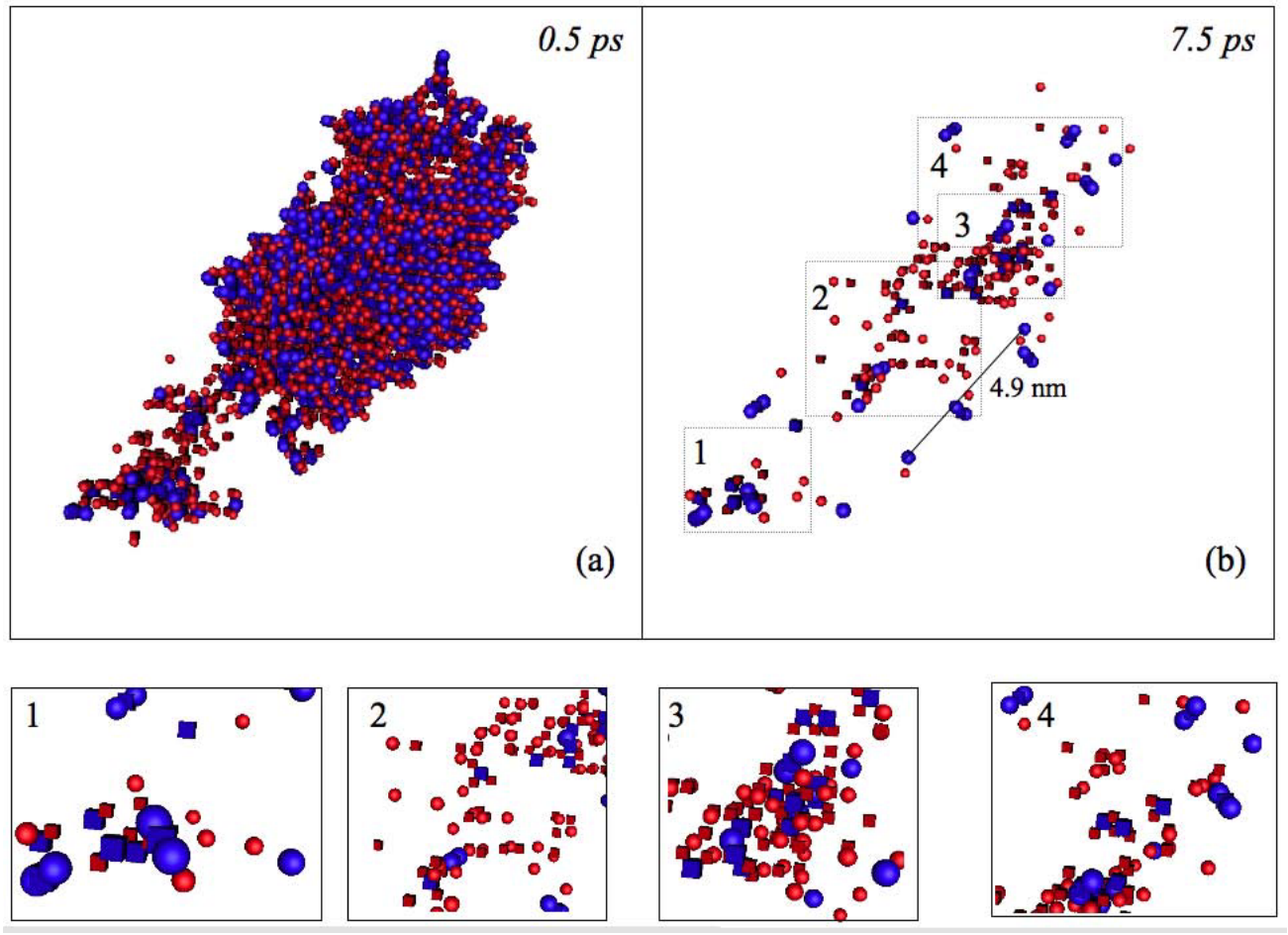

Figure 6. (Colour online) Snapshots of a 10 keV collision cascade initiated by an Er PKA. (a) The defects near the time of peak damage, 0.5 ps and (b) the defects after the end of the ballistic phase, 7.5 ps. (1)–(4) are zoomed images from (b).

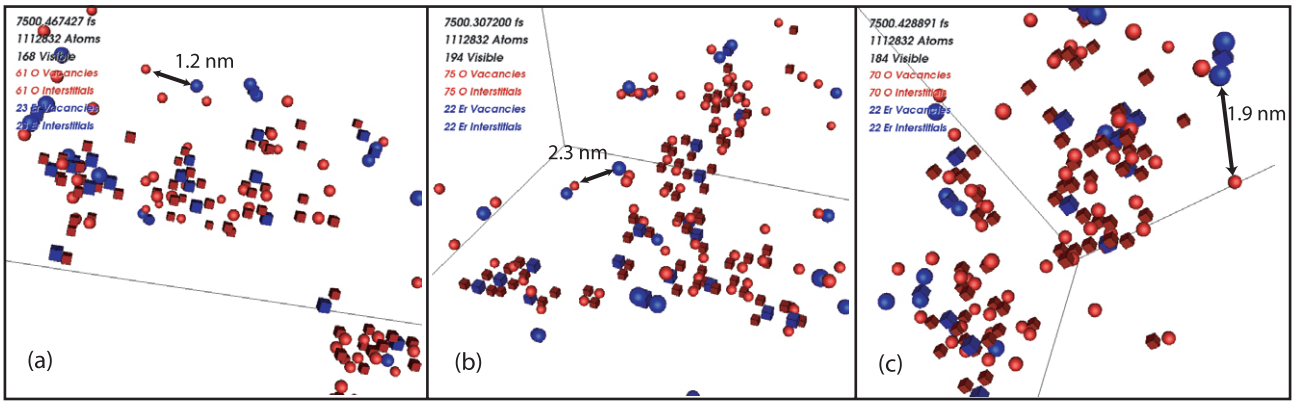

Figure 7. (Colour online) Snapshots of a 10 keV collision cascade initiated by an Er PKA along (a) ⟨352⟩, (b) ⟨432⟩ and (c) ⟨513⟩ directions.

4.2. Oxygen interstitial

The minimum energy oxygen interstitial is found in a structural vacancy site (16c). There are three possible pathways for the oxygen interstitial to move, with energy barriers of 1.44, 2.15 and 2.29 eV (see table 2). These are higher than those for the oxygen vacancy. The pathways of motion are shown in figure 9. Figure 9(a) shows that the oxygen interstitial can move directly to the nearest structural vacancy site with the smallest energy barrier of 1.44 eV. Figures (b) and (c) show pathways which have higher energy barriers of 2.15 and 2.29 eV. These processes require two atoms to move. First the oxygen atom labelled 1 moves to occupy the structural vacancy and then the oxygen interstitial moves to site 1. As in the transition of oxygen vacancy, since the smallest energy barrier is only an exchange mechanism between similar sites, net diffusion through the lattice requires the second-lowest

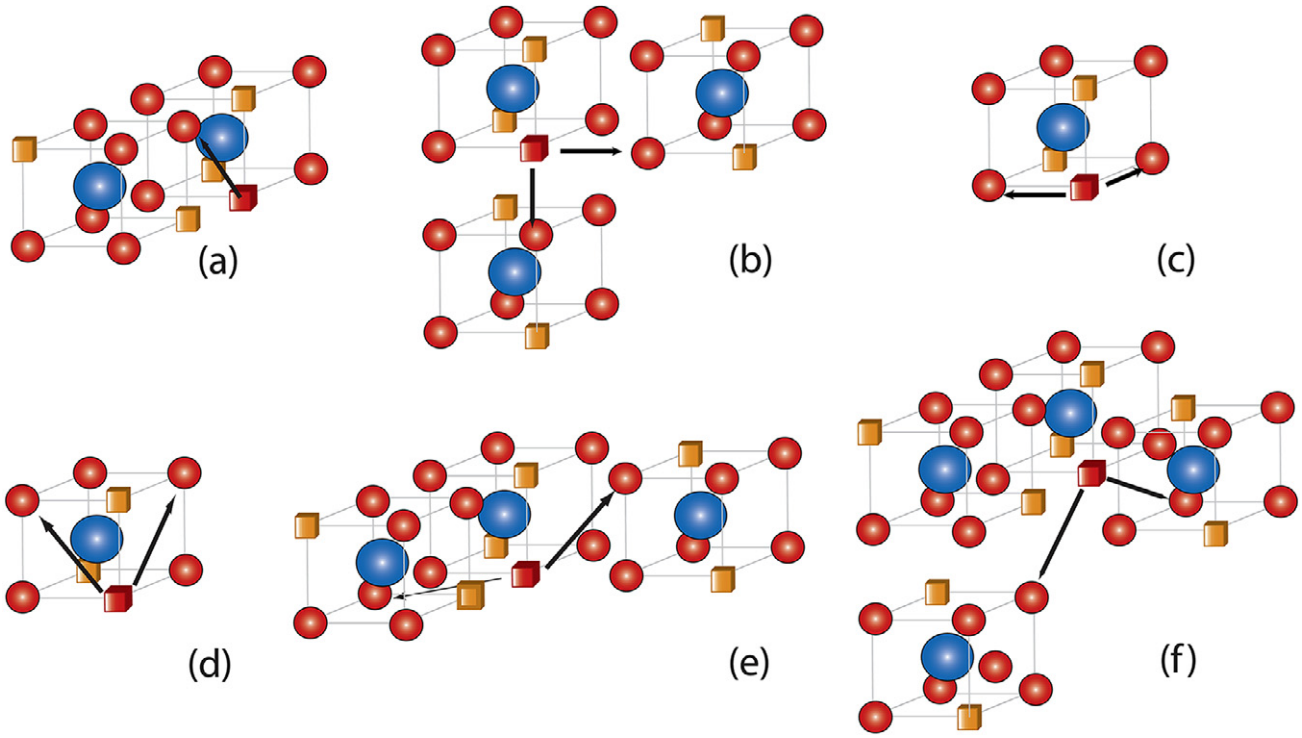

Figure 8. (Colour online) Motion of the oxygen vacancy can occur via multiple pathways. (a)–(c) are the most dominant transitions with energy barriers of 0.8, 1.01 and 1.37 eV. (d)–(f) are rarer transitions which have higher energy barriers of 1.94, 1.97 and 2.31 eV, respectively.

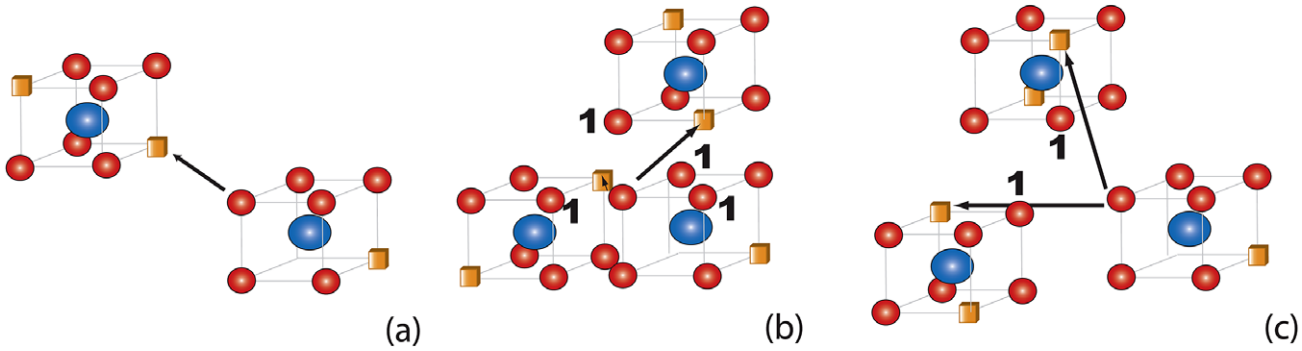

Figure 9. (Colour online) The motion of the oxygen interstitial occurs via three paths. (a) has the smallest energy barrier of 1.44 eV. Here the oxygen interstitial moves to the nearby vacancy structural site directly. (b) and (c) are pathways which have energy barriers of 2.15 and 2.29 eV where the interstitial first moves to site 1 and displaces the O atom at site 1 to the structural vacancy position.

Table 2. Transition energy barriers for the oxygen vacancy and oxygen interstitial.

Oxygen vacancy		Oxygen interstitial	
Energy barrier (eV)	Number of different pathways	Energy barrier (eV)	Number of different pathways
0.81	1	1.44	1
1.01	2	2.15	6
1.37	2	2.29	3
1.94	2		
1.97	2		
2.31	2		

barrier to be overcome. The fact that the oxygen vacancy has a lower energy barrier for diffusion than the oxygen interstitial is different from work in MgO and spinel but consistent with studies in UO_2 and may be a general feature of fluorites and their derivatives.

4.3. Er interstitial and the split Er interstitial

The split Er interstitial and the Er interstitial at a structural vacancy are shown in figures 10(a) and (b). The split Er interstitial has a total energy lower than the non-split form by

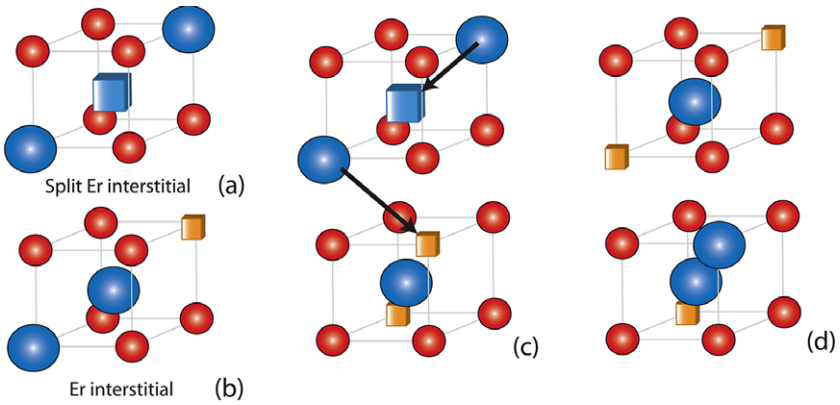

Figure 10. (Colour online) Diffusion of the Er interstitial and the split Er interstitial. The split Er interstitial shown in (a) first moves to be an isolated Er interstitial shown in (b) by overcoming an energy barrier of 0.21 eV, while the reverse barrier is 0.03 eV. The diffusion of the split Er interstitial from (c) to be an isolated Er interstitial (d) in the next sub-cube has an energy barrier of 2.46 eV.

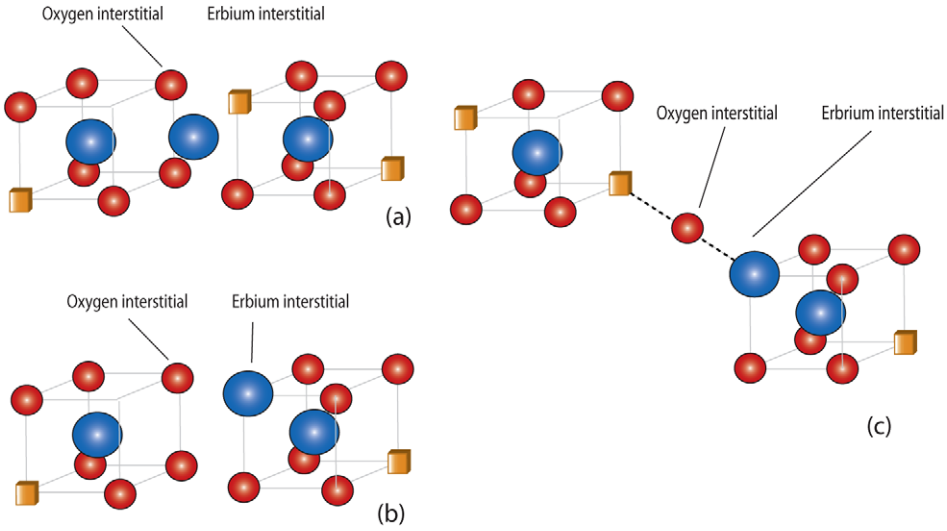

Figure 11. (Colour online) Di-interstitial structures. (a) The type 1 di-interstitial, (b) the type 2 di-interstitial, (c) the intermediate state required for net diffusion through the lattice.

0.18 eV and the energy barrier for converting from an isolated split Er interstitial to the non-split variety is 0.21 eV. In the reverse direction the barrier is 0.023 eV. Both these defects are apparent in the cascade simulations. When the Er interstitial occurs far from other defects, it most often appears as a split Er interstitial. On the other hand, if the Er interstitial is close to other defects, it is often found in the non-split form or as part of a defect cluster with oxygen interstitials in the form of di-interstitials or tri-interstitials. These will be discussed below. The diffusion of the isolated split Er interstitial to the next sub-cube has a high energy barrier of 2.46 eV. The diffusion process is shown in figure 10.

4.4. Er vacancies

There are two non-equivalent positions of the Er atom in the lattice at the 8a and 24d sites so the isolated Er vacancy can occur in two positions. Only the vacancy at the 8a site was found in the cascade simulations. The 8a position is also lower in energy by 0.9 eV. The lowest energy barrier for vacancy diffusion is 3.5 eV when moving from the 8a to 24d position. The reverse barrier is 2.7 eV.

4.5. The Er–O di-interstitials

Transitions for the di-interstitial are examined because this was highly mobile and played an important role in the accumulation of defect clusters in MgO [2]. The di-interstitials shown in figures 11(a) and (b) can be classified as first-(type 1) and second-nearest-neighbour (type 2) di-interstitials. These differ only in the position of the Er atom. In type 1, the Er atom is found between two oxygen atom sub-cube units. This is not the regular position of an Er atom observed in either of the Er interstitial sites discussed above. In type 2, the Er atom resides in a structural vacancy (16c) as for the non-split isolated Er interstitial. Type 2 has a lower energy than type 1 by 0.85 eV, and the energy barrier to move from type 1 to type 2 is 1.22 eV. The lowest energy barrier found for net diffusion was a three-step process where the rate limiting energy barrier involved is the movement of one of the O atoms as shown in figure 11(c).

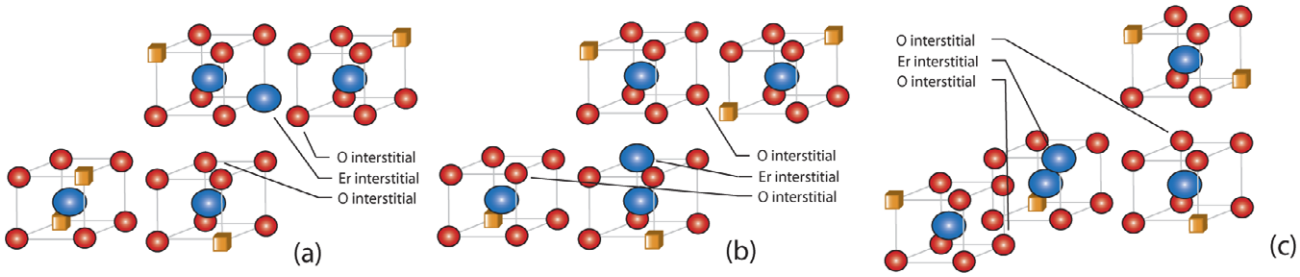

Figure 12. (Colour online) Stages in the diffusion of the O–Er–O tri-interstitial. (a) The initial positions of the interstitial atoms in the lattice. In (b) and (c) the atoms also occupy structural vacancy sites and the geometrical arrangement shown in (c) is effectively equivalent to that shown in (a).

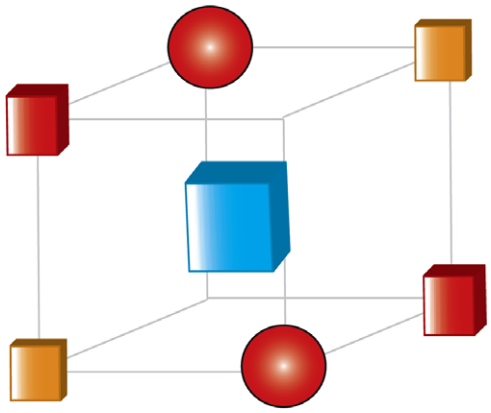

Figure 13. (Colour online) The minimum energy structure of the tri-vacancy.

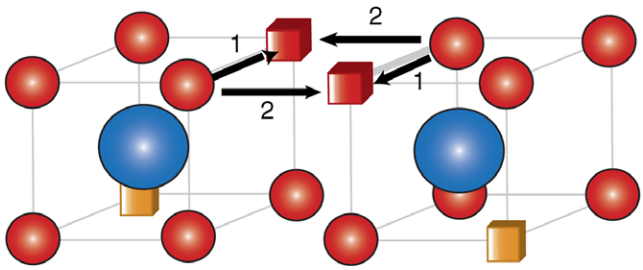

Figure 14. (Colour online) The O-square defect. Oxygen atoms can move back to their original lattice sites in two ways. The first way is following arrow 1 with an energy barrier of 0.78 eV. The second path is by following arrow 2 with energy barrier of 0.54 eV.

The energy barrier to move to this position from the type 2 configuration was found to be 2.15 eV, the same limiting value as for the isolated O interstitial. This was not expected, as in the isolated case the Er interstitial was less mobile. The energy barriers to move back from the state shown in (c) are 0.51 and 0.7 eV, respectively, for moving to type 1 and type 2. The other two steps of the diffusion process have lower energy barriers of 0.7 and 1.22 eV. Thus in contrast to MgO the di-interstitial in Er_2O_3 will not diffuse easily, even at elevated temperatures, and does not move in a concerted way with the rate limiting process being the O atom movement.

4.6. The O–Er–O tri-interstitial

The tri-interstitial is shown in figure 12(a). The rate limiting barrier for net diffusion of this structure is again the motion of the O interstitial. This is the motion from the arrangement shown in figures 12(a) and (b). The barrier is 2.2 eV, slightly higher than that for the isolated O interstitial and the di-interstitial. The other steps in the diffusion process have barriers of 0.5 eV or less.

4.7. Er–O di-vacancies

Using TAD no net diffusion of the di-vacancy was found. Instead the O vacancy could move around the surrounding Er vacancy but not separate from it. There are two pathways by which the O vacancy can move around the Er vacancy, located at the 8a position. The first path has the lower energy barrier of 1.33 eV and the second path has the higher energy barrier of 1.78 eV. This result indicates that isolated Er vacancies could effectively trap the more mobile O vacancies as they diffuse through the lattice.

4.8. Tri-vacancy

The minimum energy configuration for the tri-vacancy is shown in figure 13. No net diffusion of the tri-vacancy was found from the TAD investigation. As with the di-vacancy, oxygen vacancies can move around the Er vacancy with energy barriers between 0.1 and 1.54 eV but these are trapped by the Er vacancy and do not separate over the timescales investigated.

4.9. O-square defect

A common defect seen in the MD simulations is one in which the vacancies and interstitials in the configuration lie on the vertices of a square. We adopted the name 'O-square' for this defect. This defect has some similarity with the ring defect observed in spinels in which three aluminium atoms are displaced into adjacent structural vacancy sites so that the resulting vacancy–interstitial complex looks like a ring [4–6]. The O-square formation can be explained easily by two oxygen atoms moving to occupy tetrahedral interstices in adjacent sub-cubes (figure 14). The defect occurs often in collision cascades as shown in figure 4. The formation energy for an

Table 3. The diffusion constants for O vacancy and O interstitial as a function of temperature.

Oxygen vacancy (O_V)		Oxygen interstitial (O_I)	
Temperature (K)	D (m^2 s^{-1})	Temperature (K)	D (m^2 s^{-1})
4000	2.7×10^{-8}	4000	4.2×10^{-9}
3000	8.4×10^{-9}	3000	4.6×10^{-10}
2000	8.5×10^{-10}	2000	5.3×10^{-12}
1000	1.2×10^{-12}	1000	7.6×10^{-18}

isolated O-square defect is 4.6 eV. The defect can recover to the perfect lattice in two distinct ways. The first way is that the two oxygen interstitials move following pathway 1 in figure 14. This has an energy barrier of 0.78 eV while the reverse energy barrier to form the defect in the first place is 5.3 eV. The second path, labelled 2 in figure 14, is where oxygen atoms cross into the adjacent sub-cubes. This barrier is 0.54 eV with a reverse energy barrier of 5.1 eV. The large difference between the formation energy and the reverse energy barriers indicates that the O-square could absorb energy from a collision cascade while releasing the energy as it reverts to the perfect crystal position over longer timescales. Although the O-square appears often in the cascades it does not appear to be related to any of the structural transformations observed experimentally since the local density of atoms remains the same and a densification is observed experimentally.

5. Diffusion constants

Because the diffusion of point defects involves multiple pathways and not just one process, KMC is used to determine the diffusion constants. KMC can access much longer timescales than TAD and, as such, allows for better statistical sampling. However since the KMC here is not self-learning, it has the limitation that all possible events must be supplied *a priori*, which here we take from the TAD simulations. Results for the oxygen interstitial and vacancy are given since not only are they the simplest point defects, they also have the lowest energy barriers for diffusion. The barriers for the transition pathways determined from the TAD study were used in the KMC simulation (see table 2). To calculate the diffusion constant a large enough value for the interval time t_{sample} needs to be chosen to ensure convergence. This is determined by trial and error since it depends on both the temperature of the simulation as well as the particular defect under investigation. To ensure convergence, t_{sample} was increased until the value for the diffusion constant did not change. Two significant figures are chosen for convergence. In the calculation a constant prefactor of $\nu_0 = 10^{13}$ was chosen as an initial estimate obtained from TAD. The values for the diffusion constants are given in table 3. The diffusion constants for both defects follow exactly an Arrhenius relation. Although a constant prefactor of $\nu_0 = 10^{13}$ was chosen, initial estimates for the O vacancy using a combination of TAD and the Vineyard method [21] show a range of different values, namely 1×10^{13}, 4×10^{12}, 7×10^{12} and 1×10^{13}, for the 0.8 eV, 1.01 eV, 1.37 eV and 1.94 eV energy barriers, respectively.

During the diffusion process the oxygen vacancy (O_V) and interstitial (O_I) must overcome the second-lowest energy barrier before they can move through the lattice. The lowest energy barrier describes only a single hop back and forth between adjacent states. At 300 K, the O_V moves via the minimum energy barrier, 0.8 eV, for 99.97% of all attempts while it chooses the second minimum energy barrier for only 0.03% of attempts. Thus at room temperature the O_V will oscillate several thousand times before moving to the next state. The timescale for a hop with an energy barrier higher than 0.8 eV is about 1 h. At 1000 K, the probability of executing the minimum energy barrier is decreased to 86.89% while the second minimum energy barrier is chosen in 12.96% of all attempts. The O_I, at 300 K, chooses the minimum energy barrier to move in more than 99.99% of all attempts with a very small probability to move via any other energy barrier. At 1000 K, the probability to move via the minimum energy barrier decreased to 99.91%. The O_I defect is effectively immobile at room temperature but the small energy difference between the second-and third-lowest energy barriers means that both of these transitions are activated at about the same higher temperature.

6. Discussion and conclusions

The simulation of radiation damage in sesquioxide Er_2O_3 has shown that there are significant differences between this material and other oxides such as MgO or $MgAl_2O_4$. The large mass difference between the two ion species results in collision cascades with different structures dependent on the species of the PKA. The most mobile point defect is the O vacancy, in contrast to the other materials where the interstitials are more mobile. In addition the energy barriers for diffusion are much higher in Er_2O_3. Although only single radiation events have been investigated in this study it suggests that (low dose) radiation-induced damage would be frozen at the end of the ballistic phase of the cascade as a result of the high energy barrier for diffusion of point defects and small clusters. Although the high energy barriers mean that the material might not readily return to its crystalline state after an irradiation event the relaxation kinetics of the complex structures observed in some of the cascades might be very different from the isolated defects. *Ab initio* calculations with other oxides suggest that the fixed charge models overestimate the binding energies of defects but that agreement with the energy barriers is much better [2, 3].

If the high energy barriers for recovery were also characteristic of the more damaged regions, it suggests that Er_2O_3 would easily amorphize or be subject to phase change after large doses of radiation. The experimental results, however, find that the material does not amorphize easily as a result of radiation. Instead the experimental results indicate a density increase in the near-surface region of irradiated Er_2O_3 after a transformation to a less symmetric crystal phase after implantation by Kr ions. This appears to occur solely as the result of a radiation-induced volume change which is the subject of ongoing investigation.

Acknowledgments

LK would like to acknowledge a Higher Education Strategic Scholarship for Frontier Research from the Royal Thai Government. The work was also supported by United States Department of Energy, Office of Basic Energy Sciences. Los Alamos National Laboratory is operated by Los Alamos National Security, LLC, for the National Nuclear Security Administration of the US DOE under contract DE-AC52-06NA25396.

References

[1] Matze H, Rondinella V V and Wiss T 1999 *J. Nucl. Mater.* **274** 47
[2] Uberuaga B P, Smith R, Cleave A R, Montalenti F, Henkelman G, Grimes R W, Voter A F and Sickafus K E 2004 *Phys. Rev. Lett.* **92** 115505
[3] Gilbert C, Kenny S D and Smith R 2007 *Phys. Rev.* B **76** 184103
[4] Smith R, Bacorisen D, Uberuaga B P, Sickafus K E, Ball J A and Grimes R W 2005 *J. Phys.: Condens. Matter* **17** 875
[5] Bacorisen D, Smith R, Uberuaga B P, Sickafus K E, Ball J A, Grimes R W and Uberuaga B P 2006 *Phys. Rev.* B **74** 214105
[6] Bacorisen D, Smith R, Ball J A, Grimes R W, Uberuaga B P, Sickafus K E and Rankin W T 2006 *Nucl. Instrum. Methods* B **250** 36
[7] Uberuaga B P, Bacorisen D, Smith R, Ball J A, Grimes R W, Voter A F and Sickafus K E 2007 *Phys. Rev.* B **75** 104116
[8] Tang M, Valdez J A, Lu P, Gosnell G E, Wetteland C J and Sickafus K E 2004 *J. Nucl. Mater.* **328** 71
[9] Tang M, Lu P, Valdez J A and Sickafus K E 2006 *J. Appl. Phys.* **99** 063514
[10] Tang M, Lu P, Valdez J A and Sickafus K E 2006 *Nucl. Instrum. Methods* B **250** 142
[11] Tang M, Lu P, Valdez J A and Sickafus K E 2006 *Phil. Mag.* A **86** 1597
[12] Tang M, Valdez J A, Sickafus K E and Lu P 2007 *JOM* **59** 36
[13] Tang M, Lu P, Valdez J A, Stanek C R and Sickafus K E 2007 *Phys. Status Solidi* c **4** 1171
[14] Kittiratanawasin L, Smith R, Uberuaga B P, Sickafus K E, Cleave A R and Grimes R W 2008 *Nucl. Instrum. Methods* B **266** 2691
[15] Catlow C R A, Freeman C M and Islam M S 1988 *Phil. Mag.* A **58** 123
[16] Greengard L and Rokhlin V 1985 *J. Comput. Phys.* **60** 187
[17] Sørensen M R and Voter A F 2000 *J. Chem. Phys.* **112** 9599
[18] Jønsson H, Mills G and Jacobsen K W 1998 *Classical and Quantum Dynamics in Condensed Phase Simulations* ed B J Berne, G Ciccotti and D F Coker (Singapore: World Scientific) p 385
[19] Du D C, Devanathan R, Corrales R, Weber W J and Cormack A N 2006 *Phys. Rev.* B **74** 214204
[20] Geisler T, Trachenko K, Rios S, Dove M T and Salje E K H 2003 *J. Phys.: Condens. Matter* **15** L597
[21] Vineyard G H 1957 *J. Phys. Chem. Solids* **3** 121